Insertion loss of a multi-plane light conversion device with few mode fiber outputs under atmospheric conditions

Sarah A. Tedder*[a], Brian E. Vyhnalek[a], Yousef K. Chahine[a], and Bertram Floyd[b]

[a]NASA Glenn Research Center, 21000 Brookpark Rd, Cleveland, OH, USA 44135-3127;
[b]Hx5 Sierra, 21000 Brookpark Rd, Cleveland, OH, USA 44135-3127;

ABSTRACT

A key challenge of photon counting optical communication is delivering light with atmospherically distorted wavefronts from the telescope to detectors efficiently. When using fiber coupled single photon detectors, the efficiency of the transmittance is constrained by the modes supported by the fiber. The number of modes supported by a fiber depends on the size of the core. The larger the core, the more modes supported. However, commercial off the shelf superconducting nanowire single photon detectors (SNSPDs) are currently limited in area, which limits the core size of the fibers that can efficiently couple to the detectors. To increase the amount of light that can be delivered to the detectors, NASA Glenn Research Center is considering many different fiber/detector architectures. This paper compares insertion loss of the fiber device for two different architectures:

- a multi-plane light conversion device to split the light from a 30 µm core diameter fiber into 7 separate, 15 µm core diameter few-mode fibers butt-coupled to 7 single-element SNSPDs, and

- a 30 µm core diameter multimode fiber butt-coupled to a 16 multi-element, SNSPD array.

The measured insertion loss for each fiber device under emulated atmospheric conditions with D/r_0 between 2 and 30 is presented. The multi-plane light conversion device shows a consistent ~1 dB loss more than the multimode fiber. Also presented is the measured uneven power splitting of the multiplane light conversion device, especially at lower D/r_0. How this uneven power splitting contributes to system loss called blocking loss is discussed.

Keywords: Multi-plane light conversion device, fiber coupling, free-space optical communications, photon counting, and ground receiver.

1. INTRODUCTION

Future NASA science and exploration missions will expect increased data volumes necessitating increased instantaneous data-rate demands from NASA communications systems. The significant benefits of optical links compared to the radio-frequency (RF) communications systems currently in operation, namely the potential for 10s – 100s times more data capacity, reduced size, weight, and power (SWaP), as well as an unregulated spectrum make optical communications systems very promising solutions. In addition to the intrinsic reduction in spacecraft burden, further savings in SWaP can be achieved through improvements in ground receiver sensitivity, i.e. with advancements in areas such as photodetector technology, telescope coupling, system design, etc. For missions operating on photon-starved channels in which the received signal is faint enough to require direct-detection with single photon-counting detectors, particularly deep-space applications, each component must be optimized for highest efficiency.

For operating wavelengths around 1550 nm, superconducting nanowire single-photon detectors (SNSPDs) significantly outperform semiconductor InGaAs photodetectors and photomultiplier tubes (PMTs) in terms of detection efficiency, dark counts, speed, and timing resolution, with the drawback of requiring cryogenic cooling on the order of a few kelvin or less, depending on material. A SNSPD-based receiver was successfully demonstrated in 2013 with NASA's Lunar Laser Communications Demonstration (LLCD)[1], and both the upcoming Deep Space Optical Communications (DSOC)[2] and Orion Artemis II Optical Communications System (O2O)[3] programs will utilize SNSPD-based receivers. In addition, several commercial vendors offer multichannel SNSPD systems with simplified cryogenics, thus reducing the engineering load and increasing the viability of such systems for operational deployment.

*sarah.a.tedder@nasa.gov;   phone 1 216 433-6591; nasa.gov

An important consideration for the design and development of optical receivers based on cryogenic SNSPDs is coupling from the telescope to the detector(s). Although both free-space coupling and fiber-optic coupling have respective advantages and challenges, fiber coupling offers a more flexible receiver design, and is more typical for commercial detector systems. For the high-photon efficiency (HPE) optical receiver under development at the NASA Glenn Research Center[4], several fiber-to-SNSPD architectures are being investigated. These architectures include a graded index multi-mode fiber (GI-MMF) coupled to commercial multielement SNSPD arrays[5], and the system depicted below in Figure 1, in which a fiber device coupled to the receiver telescope splits the light to multiple individually fiber-coupled SNSPDs.
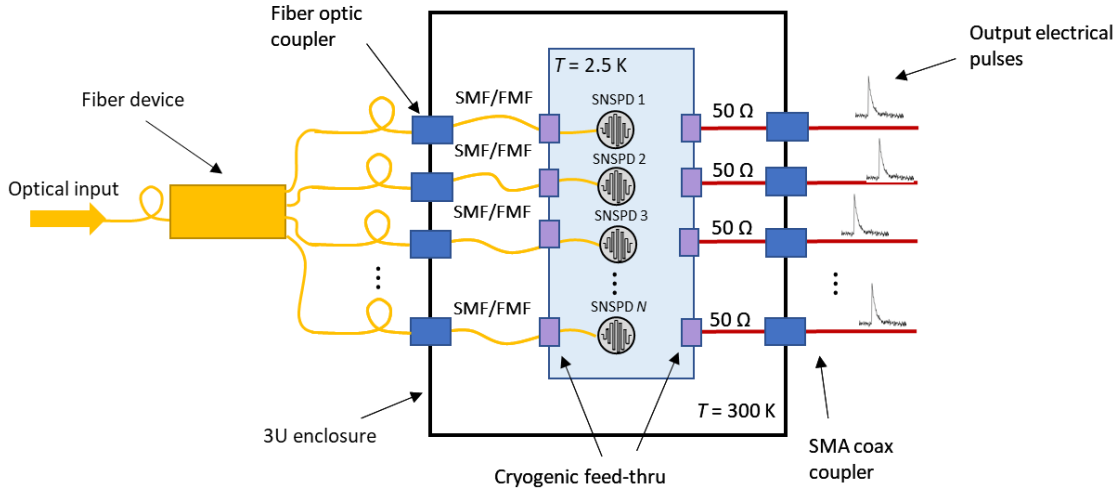

Figure 1. Fiber-coupled multichannel single-photon detector system

Ground-based receivers must contend with atmospheric effects on the transmitted beam, particularly turbulence-induced phase perturbations which distort the initial transmitted Gaussian profile scattering energy into high-order spatial modes. While adaptive optics (AO) can certainly reduce this effect, generally it is very challenging or in some instances not possible to implement AO on a photon-starved communication channel[6]. Thus, assuming passive telescope coupling, for highest efficiency the fiber core must be able to accommodate the range of modes expected based on the anticipated astronomical seeing, or the corresponding atmospheric coherence length, r_0 at the ground station. However, the typical characteristic scale of an SNSPD is on the order of the mode field diameter of single-mode fiber, as large-area SNSPDs have fabrication challenges, thus are typically coupled with minimal loss to single-mode fiber (SMF)[7], or FMF having similar mode field diameter[8]. As a potential solution for both efficient telescope coupling, as well as efficient coupling to multiple FMF-coupled SNSPD channels, we have previously investigated photonic lanterns[9], in which multiple output SMFs or FMFs are adiabatically tapered to form a single multi-moded input core such that the total number of guided modes in the output ports sum to the number of guided modes in the MMF input port.

Another potential alternative, investigated here, is a fiber-coupled multi-plane light conversion (MPLC) device. The principle of MPLC is that any unitary transformation[10] of an input optical field can be accomplished through multiple successive transmission through, or reflection from, phase-sensitive components with interleaved free-space propagation or lenses to perform optical Fourier transform operations. Phase-sensitive components that can be used include deformable mirrors[10], phase plates, or spatial light modulators[11]. For satellite-to-ground applications, the MPLC is operated as a spatial mode demultiplexer[12], similar to the photonic lantern as described above, in that input from a FMF or MMF is decomposed into multiple output fibers, typically SMF. Here we present results of insertion loss measurements of a commercial MPLC device, customized for transmitting light from a 30-μm diameter core GI-MMF into 7 FMF output fibers, under various emulated atmospheric turbulence conditions, and compare to the insertion loss of our receiver architecture baseline of a graded-index 30-μm GI-MMF.

2. EXPERIMENTAL SETUP

The characterization data presented in this paper of a GI-MMF and MPLC device were measured using the optical setup shown in Figure 2. In Figure 2, a linearly polarized fiber-coupled 1550 nm laser is used as the light source. The light exiting the polarization maintaining single-mode fiber is collimated with an 80 mm focal length collimator to a 14.5 mm diameter beam. The linear polarization direction of the light was then aligned to match the required input polarization of the polarization sensitive spatial light modulator (SLM) using a half-wave plate (HWP). The light is then passed through the 50:50 beam splitter (BS1) with half of the light reaching the 15.36 × 9.6 mm surface area of the SLM comprised of an array of 1920 × 1200 active liquid crystal elements with 8 μm pixel pitch. The phase and amplitude of the collimated beam is modulated by the SLM using a complex-amplitude phase hologram to emulate a beam after propagation through the atmosphere[13,14]. A circular aperture was emulated on the SLM by defining phase holograms truncated to a diameter set to 66.5% of the linear dimension of the central 1200 × 1200 pixel active area of the SLM corresponding to a 6.4 mm pupil. The reflection off of the SLM consists of multiple diffraction orders created by the grating of the hologram.
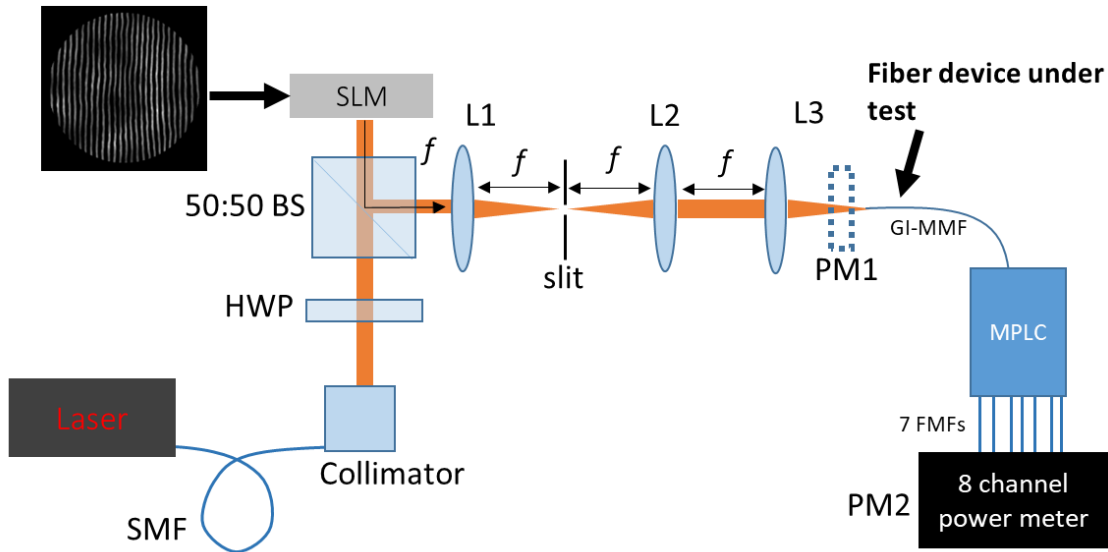

Figure 2: Schematic of the experimental setup for measuring the insertion loss of each device (not to scale).

A 4 f system with spatial filtering in the focal plane is then employed to relay the optical field at the SLM plane to the plane of L3 with only the first order reflection transmitted. Specifically, the modulated beam reflected from the SLM travels back through BS1 sending half of the remaining power into a $f = 79$ mm focusing lens (L1) placed 1 focal length from the SLM. The angle of BS1 is rotated to pass only the first order reflection through an 88 μm slit placed at the focus of L1. The light is then collimated with a second 79 mm lens (L2) placed yet another focal length f from the focal plane of L1.

The best input NA of the light at each turbulence level was identified by testing with a range of effective NAs of the input light. This was done by varying the focal lengths of the focusing lens, L3. The range of focal lengths used are shown in Table 1. These focal lengths were used with a 6.4 mm beam to produce the corresponding effective NAs listed in Table 1.

Table 1: Focal lengths of lenses used to produce the corresponding effective numerical apertures.

Focal length, mm	10	12	15	20	25	32	40
Numerical Aperture	0.32	0.27	0.21	0.16	0.13	0.10	0.08

The device is placed at the focal point of the focusing lens with a three-axis linear fine positioner. For this alignment, a hologram was applied for the SLM that produced a flat-top beam with flat phase profile. To determine the efficiency, the input power is measured with a power meter (PM1) having a 9.7 mm × 9.7 mm active surface just after the focusing lens, L3. The output power is measured with an 8-channel power meter (PM2) at the exit of the fiber or MPLC. The insertion loss was determined by taking the difference between the input and output power. Control of the SLM to apply holograms and collect power from the power meters was automated to allow the collection of 100 samples of emulation atmosphere at each turbulence level.

The range of turbulence conditions tested were D/r_0=2, 4, 10, 20, and 30, where r_0 is the atmospheric coherence length, and D is the diameter of the collection aperture. The holograms were generated based on phase and amplitude profiles generated using the split-step beam propagation method to simulate a beam propagating through slant-path turbulence. The simulations assume a 60 degree elevation angle with multiple phase screens distributed based on the Hufnagel-Valley turbulence profile up to an altitude of 24 km (*i.e.* vacuum propagation is assumed above 24 km)[13,14]. The Hufnagel-Valley profile was configured to produce r_0=20 cm and Rytov parameter of 0.02 for $D/r_0 < 10$, and $r_0 = 10$ cm with Rytov of 0.027 for $D/r_0 \geq 10$ by adjusting the structure constant at ground level assuming a 21 m/s rms upper atmospheric wind speed. For each turbulence condition D/r_0, 100 independent Monte Carlo simulations were performed to generate static samples of the atmospherically distorted beam. The simulated phase and intensity profiles were then encoded into 100 complex amplitude phase holograms on the SLM enabling the emulation of the atmospherically distorted phase and intensity. Most of the data presented were collected with holograms encoded to remove the tip/tilt of the profiles to emulate correction provided by a fast steering mirror.

2.1 Multi plane light conversion device

The MPLC device measured in this paper is a TILBA-R-CUSTOM from CAIlabs. designed to supported 1550 nm light. The input light is transmitted to the MPLC through a 10-meter graded index multimode fiber (GI-MMF). The GI-MMF has a 30 micron diameter core, an input NA of 0.2 and supports the first 21 LP fiber spatial modes (counting degeneracies). The MPLC device is designed to support the first 21 LP fiber modes and to split this light to the first 3 LP modes of the 7 output few mode fibers (FMF). The FMFs are step-index and have a 15 micron diameter core supporting the first 6 spatial modes, LP_{01}, LP_{11a}, LP_{11b}, LP_{21a}, LP_{21b}, and LP_{02}. Table 2 summarizes the specifications of the device and fibers. To determine the insertion loss caused by the MPLC and to compare to the alternate receiver architecture, a 10 meter GI-MMF matching the input fiber of the MPLC was also tested.

Table 2: MPLC device and Multi Mode Fiber Tested

Fiber	Input Core Size, μm	Input Numerical Aperture	# of LP modes supported (counting spatial degeneracies)
Step Index Few-Mode Fiber	15	0.17	6
Graded Index Multi-Mode Fiber	30	0.2	21
TILBA-R-Custom	30	0.2	21

3. RESULTS AND DISCUSSION

This section presents the results of the measured insertion loss of the MPLC and MMF from low turbulence levels of D/r_0=2 up to a higher level of 30. How the best input NA for minimum insertion loss varies with D/r_0 for both devices is presented first. Next, at the best NA identified for each turbulence condition, the variance of the insertion loss of the fiber devices over the range of D/r_0 is presented and compared, revealing the additional insertion loss caused by the MPLC. The trends presented are for an emulation with the tip/tilt removed as would be the case for a system using a fast steering mirror (FSM). To provide a snapshot of the effect of not using a FSM, results are presented at D/r_0=10 with no tip/tilt removal. Finally, the distribution of the power split of the MPLC's output fibers is presented and potential impacts to the system are discussed.

3.1 Variance of best input numerical aperture with turbulence

To identify the NA that minimizes the free space light insertion loss to the fiber devices, the devices were measured over a range of NAs at each D/r_0. The NA was varied by changing the focal length of the focusing lens (L3) in Fig. 2. The lenses NA's tested are listed in Table 1. The NA that resulted in the average minimum insertion loss is then considered the best NA. The best NA's variance with D/r_0 for both devices is plotted in Figure 3.
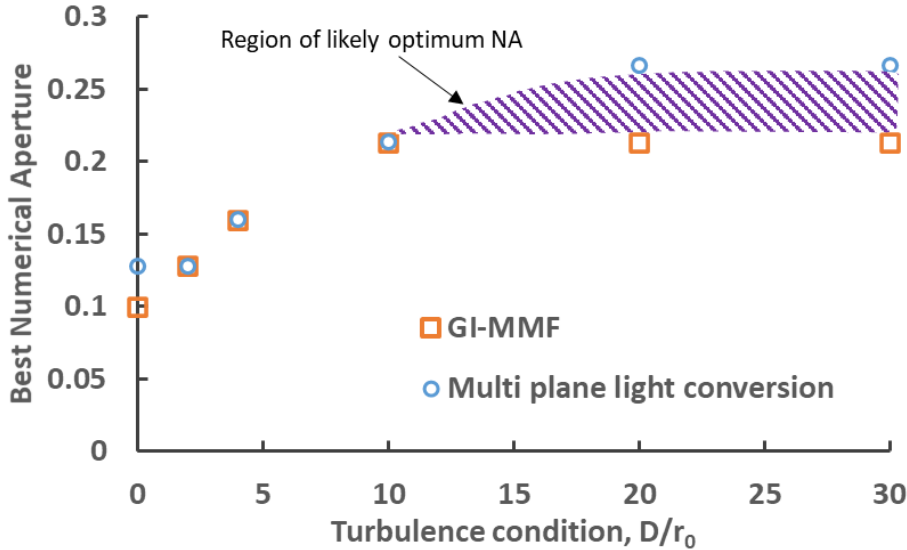

Figure 3: Best input numerical aperture for minimum insertion loss versus D/r_0 for the MPLC device (blue circles) and GI-MMF (orange squares).

In Fig. 3 the MMF's best NA, shown in orange squares, increases with D/r_0 up to 10. At higher D/r_0 the best NA for the MMF remains constant until 30. The best input NA for D/r_0 from 10 to 30 is the closest to matching the fiber's NA of 0.2. Increasing D/r_0 values corresponds to increased turbulence levels at which more energy is scattered to higher spatial modes. Fig. 3 indicates for $D/r_0 < 10$ as the energy of the beam is scattered to higher order spatial modes, larger NAs are required to optimize the overlap of the free space spatial modes to the modes supported by the fibers. Over $D/r_0 = 10$ increasing the NA seems to no longer improve this overlap. This may indicate that at $D/r_0 > 10$ the energy that fills the higher order modes are not supported by the fiber at a significant level to affect the coupling efficiency. In other words, the energy in these modes leaked from the fiber core regardless of whether the light is coupled into the fiber. Simultaneously, less energy from the lower order modes are coupled as the larger NA decreases the overlap of the mode shape with the lower order modes.

The MPLC's best NA, represented in the plot by the blue circles, is similar to the GI-MMF. In fact the best NA is exactly the same at $D/r_0 = 2, 4$, and 10. The MPLC best NA is higher than for the GI-MMF at $D/r_0 = 0, 20$ and 30. However this does not indicate a fundamental difference in performance of the MPLC and GI-MMF but reflects the narrow difference between the best NA and second best NA as shown in Figure 4. Figure 4 is a plot of insertion loss verses the input numerical aperture at $D/r_0 = 20$ for both devices. At this D/r_0 the differences between the best NA and second best NA is 0.18 dB for the MPLC device and 0.08 dB for the GI-MMF. These differences in power are well within the error of the measurements from the laser and power meters. The optimum NA is likely between these 2 NA's in the region indicated in Figure 3.
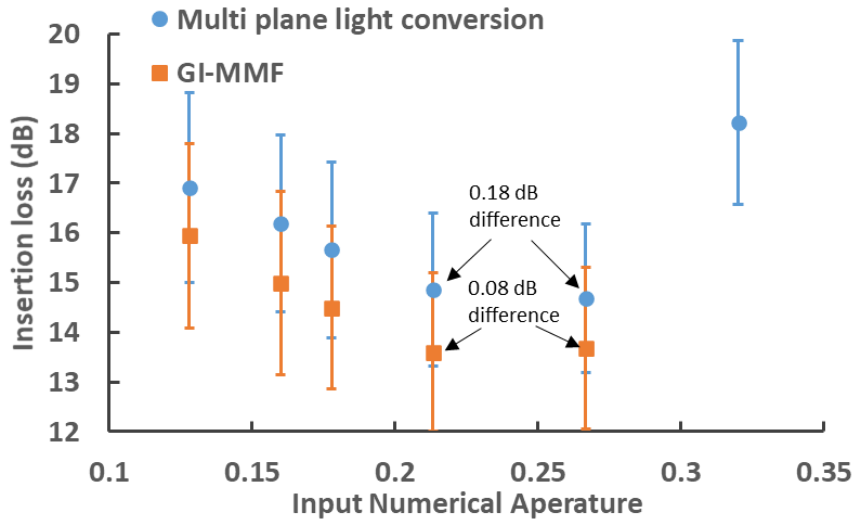
Figure 4: Insertion loss versus NA at $D/r_0 = 20$ for the MPLC device and GI-MMF. Shows the shallow minimum of the insertion loss curves. Also shows minimal difference in insertion loss between the best NA and next best NA.

3.2 Variance of insertion loss with turbulence

The minimum insertion loss at the best input NA for each D/r_0 is plotted verses $D/r0$ in Figure 5 for both devices. The symbols show the average insertion loss for 100 random atmospheric perturbations at each D/r_0, while the error bars indicate the standard deviation. The solid shapes are measured with tip/tilt correction applied. The open symbols at $D/r0 = 10$ have no tip/tilt correction. The tip/tilt correct provided a gain of ~2 dB for both devices.

All devices have increased insertion loss as higher D/r_0 conditions scatter the energy into the higher order spatial modes. The GI-MMF (orange squares) has the lowest insertion loss at all conditions. The MPLC device (blue circles) has an almost constant ~1 dB more insertion loss across the turbulence levels. The difference between the MPLC and GI-MMF insertion loss, is the added insertion loss of the rest of the components of the MPLC that follow the input GI-MMF fiber. These differences for all of the D/r_0's are provided in Table 3. Averaged across all measured D/r_0 the difference in the insertion loss of the MPLC from the GI-MMF is 1.13 dB±0.13.
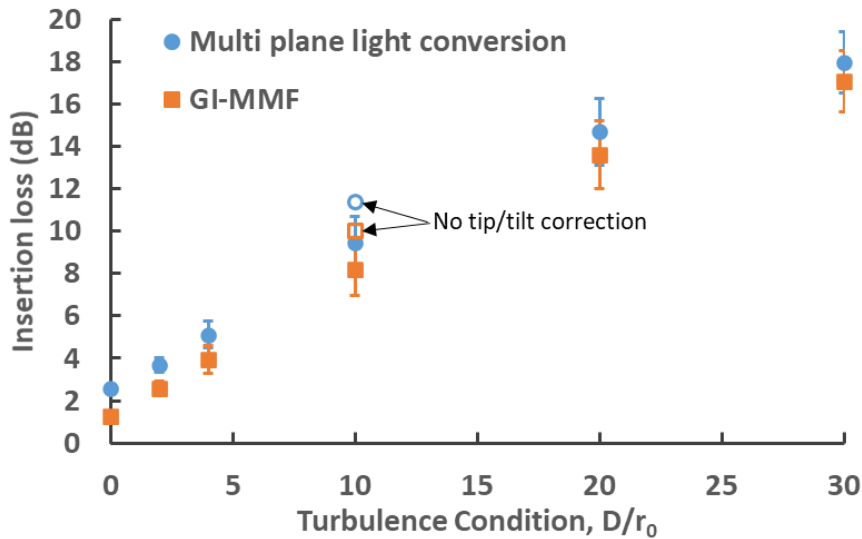

Figure 5: Plot of the input insertion loss at their best performing input NA verses the D/r_0 for the GI-MMF (orange squares), and MPLC device (blue circles). Solid shapes are tip/tilt corrected.

Table 3: Added insertion loss of the MPLC over the GI-MMF

D/r_0	Added insertion loss of MPLC (dB)
0	1.28
2	1.10
4	1.16
10	1.28
20	1.08
30	0.88

3.3 Variance of output fiber power split with turbulence

To compare the 2 fiber devices as they will perform in the receivers described in the introduction, detector blocking loss, must be considered. Detector blocking loss happens when photons are not counted because they arrive at a faster rate than the reset time of an SNSPD[15]. If an equal fraction of power is sent from the 7 FMF outputs of the MPLC device, then the blocking loss would be minimized. As shown in the Figure 6 a -d, the fraction of power of the 7 FMF output fibers favor the middle channels consistently with channel 4 being the highest fraction of power. The dashed line shows the ideal even distribution of power fraction. As the D/r_0 increases, the distribution of power become more even until D/r_0=10. At D/r_0=10 and higher, the fraction of power distribution similarly favors the middle channels. These results indicate that the blocking loss will be highest at D/r_0=2 and then decrease until D/r_0=10 and then remain constant.
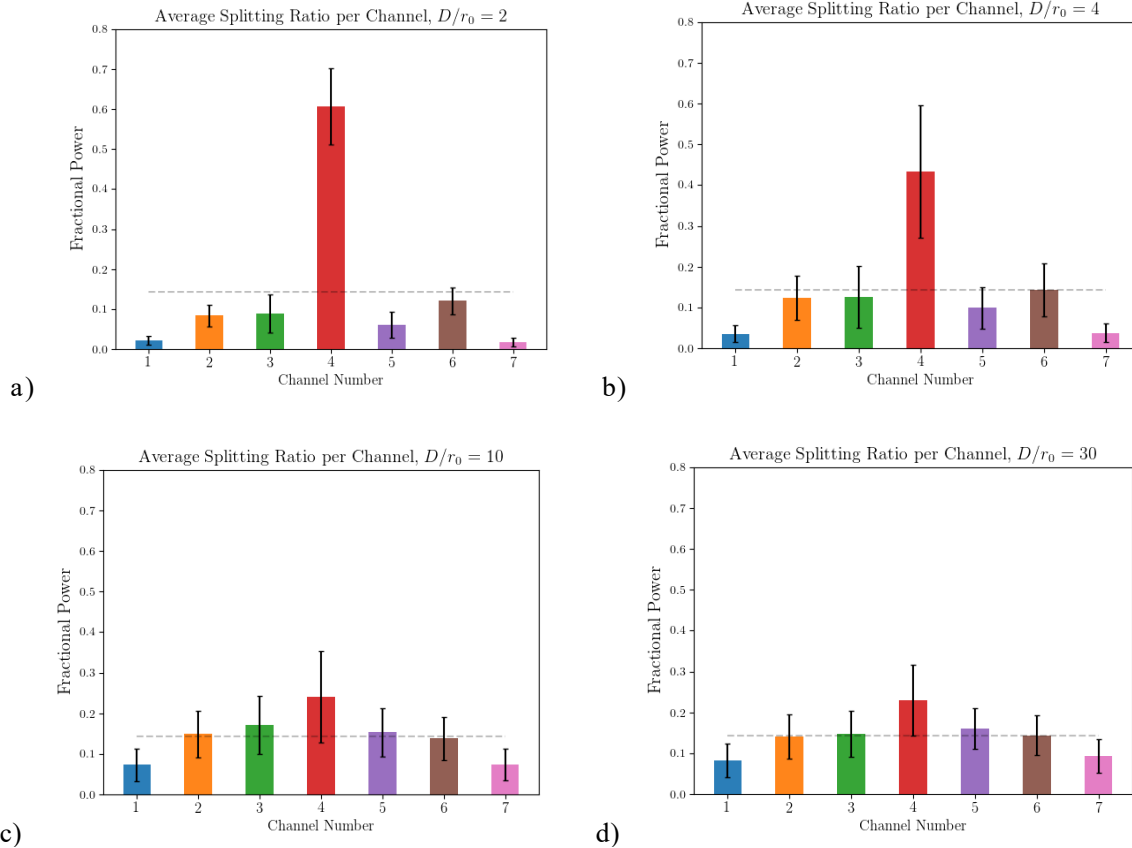
a)

b)

c)

d)

Figure 6: Bar charts showing the average and standard deviation of the fraction power output from each fiber (channel) of the MPLC device at the following D/r_0's: a) 2, b) 4, c) 10, d) 30. The dashed line represents an even split of power.

4. SUMMARY

In summary, the MPLC device has more loss than a GI-MMF although both supported 21 fiber spatial modes. When compared at a range of turbulence levels ($D/r_0 \leq 30$), the MPLC insertion loss was consistently ~1 dB more than the GI-MMF. Since the GI-MMF is the same as the input fiber as used for the MPLC, the ~1 dB loss can be attributed to losses caused by the rest of the MPLC components.

As a component of an optical ground receiver, the MPLC will also contribute loss through uneven splitting of the light to the detectors. The MPLC had an uneven power fraction split, sending more power to the middle channel output fibers. The magnitude of the uneven split decreases with increasing turbulence levels. As a result, the MPLC device will contribute more blocking loss at the lower turbulence levels. Although not measured for this paper, the GI-MMF coupled to a 16–element SNSPD array may also incur blocking losses due to non-uniformities in the intensity distribution on the detector array. However, this is highly dependent on the SNSPD array geometry.

The next step is to quantify the amount of blocking loss the measured power splits are likely to contribute. This will be done in future work by using the power splits as input into a system model described previously[16]. To give a more complete picture of the predicted performance compared to the GI-MMF architecture blocking losses will also need to be measured the future.

ACKNOWLEDGEMENTS

REFERENCES

[1] B. S. Robinson, D. M. Boroson, D. A. Burianek, D. V. Murphy, F. I. Khatri, J. W. Burnside, J. E. Kansky, A. Biswas, Z. Sodnik, and D. M. Cornwell, "The NASA lunar laser communication demonstration - successful high-rate laser communications to and from the moon," in AIAA - SpaceOps 2014, 2014.

[2] A. Biswas et al., "Status of NASA's deep space optical communication technology demonstration," 2017 IEEE International Conference on Space Optical Systems and Applications (ICSOS), 2017, pp. 23-27, doi: 10.1109/ICSOS.2017.8357206.

[3] Antonios Seas, Bryan Robinson, Tina Shih, Farzana Khatri, and Mark Brumfield "Optical communications systems for NASA's human space flight missions", Proc. SPIE 11180, International Conference on Space Optics — ICSO 2018, 111800H (12 July 2019); https://doi.org/10.1117/12.2535936.

[4] Vyhnalek, B., Nappier, J., Tedder, S., "Real Time Photon-Counting Receiver for High Photon Efficiency Optical Communications", IEEE ICSOS, (2019).

[5] Timothy. M. Rambo, Amy R. Conover, and Aaron J. Miller, "16-Element Superconducting Nanowire Single-Photon Detector for Gigahertz Counting at 1550-nm," March 2021. [Online]. Available: arXiv:2103.14086.

[6] Lewis C. Roberts Jr., Seth Meeker, Sabino Piazzola, and J. Chris Shelton "Daytime adaptive optics for deep space optical communication", Proc. SPIE 11133, Laser Communication and Propagation through the Atmosphere and Oceans VIII, 1113308 (6 September 2019); https://doi.org/10.1117/12.2524633.

[7] A. J. Miller, A. E. Lita, B. Calkins, I. Vayshenker, S. M. Gruber, and S. W. Nam, "Compact cryogenic self-aligning fiber-to-detector coupling with losses below one percent," Optics Express, vol. 19, no. 10, pp. 9102–9110, May 2011.

[8] B. E. Vyhnalek, S. A. Tedder, E. J. Katz, and J. M. Nappier, "Few-mode fiber coupled superconducting nanowire single-photon detectors for photon efficient optical communications," in Free-Space Laser Communications XXXI, H. Hemmati and D. M. Boroson, Eds., vol. 10910, International Society for Optics and Photonics. SPIE, 2019, pp. 62 – 75.

[9] S. A. Tedder, B. E. Vyhnalek, S. Leon-Saval, C. Betters, B. Floyd, J. Staffa, and R. Lafon, "Single-mode fiber and few-mode fiber photonic lanterns performance evaluated for use in a scalable real-time photon counting ground receiver," in Free-Space Laser Communications XXXI, H. Hemmati and D. M. Boroson, Eds., vol. 10910, International Society for Optics and Photonics. SPIE, 2019, pp. 69 – 78.

[10] Jean-François Morizur, Lachlan Nicholls, Pu Jian, Seiji Armstrong, Nicolas Treps, Boris Hage, Magnus Hsu, Warwick Bowen, Jiri Janousek, and Hans-A. Bachor, "Programmable unitary spatial mode manipulation," J. Opt. Soc. Am. A 27, 2524-2531 (2010).

[11] Guillaume Labroille, Bertrand Denolle, Pu Jian, Philippe Genevaux, Nicolas Treps, and Jean-François Morizur, "Efficient and mode selective spatial mode multiplexer based on multi-plane light conversion," Opt. Express 22, 15599-15607 (2014).

[12] Ramon Mata Calvo, David Allioux, Andrew Reeves, Antonin Billaud, Juraj Poliak, Olivier Pinel, Helawae Friew Kelemu, Guillaume Labroille, and Mathias Richerzhagen "Alternative passive fiber coupling system based on multi-plane light conversion for satellite-to-ground communications", Proc. SPIE 11272, Free-Space Laser Communications XXXII, 112720Q (9 March 2020); https://doi.org/10.1117/12.2546076.

[13] Chahine, Y., Tedder, S., and Vyhnalek, B., "Beam propagation through atmospheric turbulence using an altitude-dependent structure profile with non-uniformly distributed phase screens", Proc. SPIE, Free-Space Laser Communication and Atmospheric Propagation, XXXII (2020).

[14] Tedder, S., Floyd, B., Chahine, Y. K., Croop, B., Vyhnalek, B., Betters, C., Leon-Saval, S. G., "Measurements of few-mode fiber photonic lanterns in emulated atmospheric conditions for a low earth orbit space to ground optical communication receiver application", Proc. SPIE, Free-Space Laser Communication and Atmospheric Propagation, XXXII (2020).

[15] Moison, B. and Piazzolla, S., "Blocking losses on an optical communications link", Proc. IEEE International Conference on Space Optical System and Applications, (2011).

[16] Brian E. Vyhnalek, Jennifer N. Downey, and Sarah A. Tedder "Single-photon counting detector scalability for high photon efficiency optical communications links", Proc. SPIE 11272, Free-Space Laser Communications XXXII, 112721A (2 March 2020); https://doi.org/10.1117/12.2546513.